Vibronic interactions in trilobite and butterfly Rydberg molecules

Frederic Hummel [1,*] Peter Schmelcher,[2,3,†] and Matthew T. Eiles[1,‡]

[1]*Max Planck Institute for the Physics of Complex Systems, Nöthnitzer Straße 38, 01187 Dresden, Germany*
[2]*Centre for Optical Quantum Technologies, Universität Hamburg, Luruper Chaussee 149, 22761 Hamburg, Germany*
[3]*The Hamburg Centre for Ultrafast Imaging, Universität Hamburg, Luruper Chaussee 149, 22761 Hamburg, Germany*

Ultralong-range Rydberg molecules provide an exciting testbed for molecular physics at exaggerated scales. In the so-called *trilobite* and *butterfly* Rydberg molecules, the Born-Oppenheimer approximation can fail due to strong nonadiabatic couplings arising from the combination of radial oscillations and rapid energy variations in the adiabatic potential energy curves. We utilize an accurate coupled-channel treatment of the vibronic system to observe the breakdown of Born-Oppenheimer physics, such as nonadiabatic trapping and decay of molecular states found near pronounced avoided crossings in the adiabatic potential curves. Even for vibrational states localized far away from avoided crossings, a single-channel model is quantitatively sufficient only after including the diagonal nonadiabatic corrections to the Born-Oppenheimer potentials. Our results indicate the importance of including nonadiabatic physics in the description of ultralong-range Rydberg molecules and in the interpretation of measured vibronic spectra.

I. INTRODUCTION

Molecular states of Rydberg atoms and atoms or ions feature exotic binding mechanisms and offer novel opportunities to investigate fundamental physics. In ultralong-range Rydberg molecules, the Rydberg atom binds to ground-state atoms via an attractive interaction induced by the scattering of the Rydberg electron from the atoms [1–3]. In charged Rydberg molecules, the Rydberg atom binds to an ion due to long-range electrostatic interactions, leading to an avoided crossing of an attractive polarization potential and a repulsive dipole potential [4–6]. In Rydberg macrodimers, two Rydberg atoms bind at the avoided crossing of attractive and repulsive van der Waals potentials [7–9]. All of these molecules feature bond lengths on the 0.1–$10\,\mu$m scale, leading to slow vibrational dynamics which can be observed in real time [10].

Due to the high density of states in Rydberg atoms and the correspondingly small energy gaps, nonadiabatic couplings play a crucial role in Rydberg molecules. They are known to modify the vibrational spectrum of macrodimers [11] and provide a decay channel for charged Rydberg molecules [12]. In ultralong-range Rydberg molecules, nonadiabatic couplings have been considered at the level of the Landau-Zener approximation to predict electronic transitions [13]. Conical

intersections in their molecular potentials can be exploited to control atomic collisions and lifetimes over a wide range of principal quantum numbers and temperatures [14].

Ultralong-range Rydberg molecules have very unusual properties, such as oscillatory Born-Oppenheimer potentials, rapid changes of electronic character, and extreme sensitivity to external fields. Therefore they provide a unique environment to test molecular physics on slow vibrational timescales, allowing direct observation of effects arising from the entanglement of vibrational and electronic degrees of freedom and offering abundant opportunities to examine concepts of molecular physics in energetic and spatial regimes very different from those relevant for ground-state molecules. Despite these promising opportunities, an *ab initio* treatment of nonadiabatic couplings in ultralong-range Rydberg molecules has not been performed yet.

In this article we study ultralong-range Rydberg molecules in a complete coupled-channel treatment for the electronic and vibrational degrees of freedom. The arising nonadiabatic couplings lead to vibronic interactions. We focus on molecular states formed in the vicinity of the avoided crossing of the trilobite and butterfly electronic states. These polar molecules have high electronic orbital angular momentum character, and their nonadiabatic coupling can become singular. We discuss several strategies for diabatization of the adiabatic representation of the total molecular wave function in order to solve the molecular Hamiltonian.

We find that nonadiabatic corrections to the molecular potentials are crucial for an accurate interpretation of molecular spectra. This sheds new light on measurements of electron scattering phase shift relying on Rydberg molecules [15–19], as the level shifts caused by nonadiabatic corrections could be misidentified as stemming from inaccurate scattering properties. Furthermore, off-diagonal nonadiabatic couplings lead

*hummel@pks.mpg.de
†pschmelc@physnet.uni-hamburg.de
‡meiles@pks.mpg.de

to the formation of molecular states without single-channel counterparts. Their structure resembles the quantum reflection states observed in single-channel calculations [20,21], although they are classically trapped by a potential barrier created by nonadiabatic coupling. Other classes of molecular states decay nonadiabatically. Spectral signatures for the experimental observation of the vibronic interaction effects are discussed.

This manuscript is structured as follows. In Sec. II we lay out the theory and methods used throughout. Section II A introduces in detail the nonadiabatic representation before we elaborate on diabatization in Sec. II B. This is to promote and simplify adaptation of this framework for future investigations. Details of the model for ultralong-range molecules and the physical parameters are provided in Sec. II C. Section III contains the results, firstly introducing the adiabatic potential energy curves in III A, secondly considering variations in the electronic structure in III B, thirdly providing the molecular spectra in III C, and finally focusing on vibronic interactions in III D. We provide a conclusion and an outlook in Sec. IV.

II. THEORY & METHODS

We consider two atoms, one excited to a high-lying Rydberg state, separated by a large distance R along the z axis of the coordinate system. The total Hamiltonian reads (in atomic units)

$$\hat{H} = -\frac{\nabla_R^2}{2\mu} - \frac{\nabla_r^2}{2} + V_c(\boldsymbol{r}) + V_{ea}(\boldsymbol{r}, R), \qquad (1)$$

where μ is the reduced mass of the diatomic system, $\boldsymbol{r}$ is the coordinate of the Rydberg electron, V_c is the interaction between the Rydberg electron and the ionic core, and V_{ea} the interaction of the Rydberg electron with the distant ground-state atom. The last three terms of Eq. (1) form the electronic Hamiltonian $\hat{H}_e(\boldsymbol{r}, R)$. To determine the eigenstates of $\hat{H}$, we employ the *adiabatic representation* and expand the total wave function in terms of solutions of the electronic Hamiltonian [22,23],

$$\Psi(\boldsymbol{r}, R) = \sum_\alpha \chi_\alpha(R) \psi_\alpha(\boldsymbol{r}; R), \qquad (2)$$

such that the sum over R-dependent coefficients $\sum_\alpha |\chi_\alpha|^2$ can be interpreted as a vibrational wave function of the nuclei, and

$$\hat{H}_e(\boldsymbol{r}, R) \psi_\alpha(\boldsymbol{r}; R) = V_\alpha(R) \psi_\alpha(\boldsymbol{r}; R) \qquad (3)$$

defines the adiabatic electronic eigenstates ψ_α with eigenvalue V_α given a fixed nuclear configuration R. $V_\alpha(R)$ are the adiabatic potential energy curves.

A. Nonadiabatic couplings

Applying the Hamiltonian (1) to Eq. (2) and projecting out the electronic eigenstates leads to a general set of coupled-channel, radial Schrödinger equations for the vibrational motion [24],

$$\left[-\frac{\nabla_R^2}{2\mu} + V_\alpha(R) - E \right] \chi_\alpha(R) = \frac{1}{2\mu} \sum_{\alpha'} \Lambda_{\alpha\alpha'} \chi_{\alpha'}(R), \qquad (4)$$

for a total energy E and assuming zero rotational angular momentum. ∇_R indicates the derivative with respect to the radial, nuclear coordinate R. The right-hand side contains the nonadiabatic coupling operator

$$\Lambda_{\alpha\alpha'} = 2P_{\alpha\alpha'} \nabla_R + Q_{\alpha\alpha'}, \qquad (5)$$

which consists of the derivative coupling elements

$$P_{\alpha\alpha'} = \int d\boldsymbol{r}\, \psi_\alpha^*(\boldsymbol{r}; R) \nabla_R \psi_{\alpha'}(\boldsymbol{r}; R) \qquad (6)$$

and the nonadiabatic scalar coupling elements

$$Q_{\alpha\alpha'} = \int d\boldsymbol{r}\, \psi_\alpha^*(\boldsymbol{r}; R) \nabla_R^2 \psi_{\alpha'}(\boldsymbol{r}; R). \qquad (7)$$

For all practical purposes, the sum in Eqs. (2) and (4) needs to be truncated. In the *Born-Oppenheimer approximation*, all nonadiabatic terms are neglected. The right-hand side of Eq. (4) vanishes, and the resulting decoupled equations can be solved individually. In the *Born-Huang approximation*, only the diagonal nonadiabatic terms are considered. In many cases, these terms are crucial to capture qualitative corrections [25,26]. It is helpful to absorb the diagonal couplings in the potential energy curves through the definition

$$W_\alpha(R) = V_\alpha(R) - \frac{1}{2\mu} Q_{\alpha\alpha}(R). \qquad (8)$$

Note that $P_{\alpha\alpha} = 0$, due to the anti-Hermiticity of the derivative coupling operator. Since the diagonal elements $Q_{\alpha\alpha}$ are strictly negative [compare Eq. (12) below], this leads to a shift to larger potential energies $W_\alpha \geqslant V_\alpha$.

In principle, the nonadiabatic coupling elements are straightforwardly obtained from the adiabatic electronic states. However, numerical difficulties frequently arise in practice. With respect to the electronic states, the operator $\Lambda_{\alpha\alpha'}$ is Hermitian while $P_{\alpha\alpha'}$ is anti-Hermitian. Hence, $Q_{\alpha\alpha'}$ is non-Hermitian, and numerical inaccuracies or round-off errors in its computation can easily lead to an overall non-Hermitian matrix and nonphysical complex energy eigenvalues. This can be avoided by recasting

$$Q_{\alpha\alpha'} = P_{\alpha\alpha'}^2 + \nabla_R P_{\alpha\alpha'} \qquad (9)$$

and using partial integration to ensure Hermiticity of the matrix elements of the nonadiabatic coupling. To this end, let us introduce a basis of the vibrational Hilbert space $B_i(R)$, such that any R-dependent function can be conveniently expanded as

$$f(R) = \sum_i c_i B_i(R), \qquad (10)$$

with constant coefficients c_i. The matrix elements of the nonadiabatic coupling operator in this basis are

$$\int dR\, B_i B_j \Lambda_{\alpha\alpha'} = \int dR\, \left[(B_i B_j' - B_i' B_j) P_{\alpha\alpha'} + B_i B_j P_{\alpha\alpha'}^2 \right]. \qquad (11)$$

As the first term is the product of two anti-Hermitian operators in the vibrational and electronic Hilbert subspaces, respectively, and the second term is the product of two Hermitian operators, this guarantees a total Hermitian representation. It

additionally avoids the need to compute second derivatives of the electronic wave functions, because

$$P_{\alpha\alpha'}^2 = -\int d\mathbf{r} \, \nabla_R \psi_\alpha^*(\mathbf{r}; R) \nabla_R \psi_{\alpha'}(\mathbf{r}; R). \qquad (12)$$

In conclusion, we can solve Eq. (4), e.g., by performing an exact diagonalization in the electronic and the vibrational degree of freedom. In some circumstances, however, the derivative coupling elements may contain highly singular points such that Eq. (4) becomes formally ill-defined [27]. It is then reasonable to switch to a representation that circumvents such difficulties.

B. Diabatic representation

We can recast Eq. (4) in the following form:

$$\left[-\frac{1}{2\mu}(\nabla_R + \hat{\mathbf{P}})^2 + \hat{V}(R) - E \right]\boldsymbol{\chi}(R) = 0, \qquad (13)$$

where the first term is understood to contain a dressed kinetic energy operator that has absorbed all nonadiabatic couplings. Note that Eq. (13) is a matrix equation where $\hat{V}$ is a matrix that contains the V_α along the diagonal and $\boldsymbol{\chi}$ is a vector of all χ_α.

Equation (13) is invariant under unitary transformations $\hat{S}(R)$. Exact diabatization is achieved when $\hat{S}$ satisfies [28]

$$(\nabla_R \hat{S} + \hat{\mathbf{P}}\hat{S}) = 0, \qquad (14)$$

in which case Eq. (13) becomes

$$\left[\frac{-\nabla_R^2}{2\mu} + \hat{U}(R) - E \right]\tilde{\boldsymbol{\chi}}(R) = 0, \qquad (15)$$

where $\tilde{\boldsymbol{\chi}} = \hat{S}^\dagger \boldsymbol{\chi}$ is the total wave function expressed in the diabatic representation and $\hat{U} = \hat{S}^\dagger \hat{V}\hat{S}$ is the diabatic potential matrix. In general, $\hat{S}$ is not unique, but as long as there is only a single adiabatic parameter (in our case R), Eq. (14) does possess a unique solution and can be solved analytically [29]. Considering two adiabatic electronic states, $\hat{S}$ is given as a simple rotation about the angle

$$\vartheta(R) = \int_R^\infty dR' \, P_{12}(R'). \qquad (16)$$

The solution for three and four electronic states is given in Appendix D. There exist other strategies for diabatization [30–32], typically related to achieving an electronic representation that provides continuity of some physical observable, such as electronic dipole moments or charge distributions. These are especially useful if $\hat{S}$ is not known. We discuss dipole diabatization and a related approach in Appendixes B and C.

C. Ultralong-range Rydberg molecules

We consider ultralong-range Rydberg molecules of rubidium. The adiabatic potential energy curves are obtained from diagonalizing the electronic Hamiltonian in a basis of atomic states ϕ_{nlm}. These states are labeled by the principal and orbital angular momentum quantum numbers of the Rydberg atom n, l, and m, and satisfy the Rydberg atom's Schrödinger equation,

$$\left[-\frac{\nabla_r^2}{2} + V_c(\mathbf{r}) \right]\phi_{nlm}(\mathbf{r}) = E_{nl}\phi_{nlm}(\mathbf{r}), \qquad (17)$$

where $E_{nl} = -\frac{1}{2(n-\mu_l)^2}$, and μ_l is an angular-momentum-dependent but energy-independent quantum defect. These quantum defects shift the atomic states from the degenerate Rydberg manifold at energy $-\frac{1}{2n^2}$, especially those with low angular momentum $l < 3$. We use quantum defect data from [33].

The electron-atom interaction is modeled using the Fermi pseudopotential [34,35],

$$V_{ea}(\mathbf{r}, R) = 2\pi a_s(R)\delta(\mathbf{r} - R\mathbf{e}_z)$$
$$+ 6\pi a_p(R)\nabla_r \delta(\mathbf{r} - R\mathbf{e}_z)\nabla_r, \qquad (18)$$

where $a_{s(p)}$ is the scattering length (volume) in the s-(p)-wave channel. These depend on R via the semiclassical kinetic energy of the electron, $k^2 = 2E_{nl} + 2/R$. We use scattering data from [19], where the zero-energy s-wave scattering length is $a_s(0) = -15.24 \, a_0$.

To represent the electronic degrees of freedom for a Rydberg molecule formed by a Rydberg atom excited to the principal quantum number n, we include in our atomic basis all states with n and $n - 1$. From this we obtain good qualitative agreement with more accurate Kirchhoff integral methods based on the Coulomb Green's function [36,37]. This descriptive level serves our goal to quantify and elucidate the importance of nonadiabatic physics, which can be obscured by the complexity of the full molecular picture. This would include quantitative corrections to the electronic structure resulting from higher partial wave scattering [38] and the electronic and nuclear spins of both atoms [39,40]. For the potential crossing between the trilobite and butterfly states studied here, specifically for the considered quantum numbers, we do not expect electronic spin couplings to influence the molecular structure up to global energy shifts. However, at higher energies additional crossings due to additional butterfly potentials of different hyperfine character may occur; compare, e.g., Refs. [40,41].

To represent the vibrational degree of freedom, we employ B splines [42]. Due to the banded structure of the involved matrices, this is numerically very efficient. Depending on the principal quantum number, we use 500–1500 splines of order 12 and uniformly spaced knot points to converge the vibrational energies and wave functions.

To simulate an absorption spectrum, the standard experimental observable to study Rydberg molecules, we account for the dipole transition strength of the total wave function assuming a two-photon excitation from the $5s$ ground state via the $6p$ intermediate state and for the Franck-Condon factor assuming a homogeneous and isotropic gas of ground-state atoms, i.e., a uniform distribution of the initial vibrational state:

$$\sigma(E) \propto \int dR \, R^2 \int d\mathbf{r} \, \mathbf{r} \phi_{6p}(\mathbf{r})\Psi(\mathbf{r}, R), \qquad (19)$$

where the wave functions are defined in Eq. (2) and below. Specifically, only the atomic S- and D-state character of the
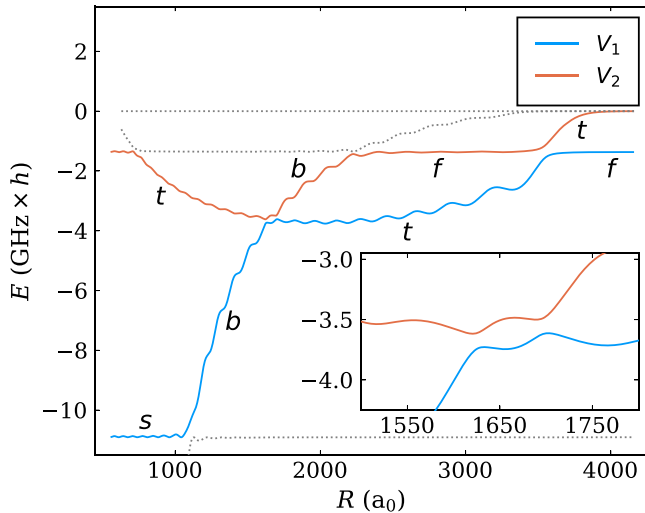
FIG. 1. Adiabatic potential energy curves V_1 and V_2 for principal quantum number $n = 43$. Other adiabatic potentials are printed as gray, dotted lines. The inset shows a zoom of the avoided crossings. Additional labels show the dominant electronic character of these adiabatic states, which varies with R: the atomic S state (s), trilobite (t), butterfly (b), and F state (f). Energies are given relative to the degenerate atomic Rydberg level.

total wave function contribute to the spectral signal. Naturally, a one-photon transition directly from the $5s$ ground state changes the spectral characteristics. Furthermore, a Gaussian profile for the line broadening of the excitation laser with a width of 1 MHz is assumed.

III. RESULTS AND DISCUSSION

In the following we present the characteristic properties of the electronic, the vibrational, and the spectral structure of neutral Rydberg molecules, taking into account nonadiabatic couplings. To illustrate the main physical phenomena, we focus on a representative subset of principal quantum numbers $n = 43$–45, through which we can elaborate on generic n-dependent features that we found studying a larger range between $n = 25$ and 70.

A. Structure of the adiabatic potential curves

Let us first consider the adiabatic potential curves shown in Fig. 1 for $n = 43$. The level structure of Rydberg molecules is such that these fall into two classes. The electronic states of dominant low-l character are, due to their quantum defects, only weakly perturbed by the interaction with the ground-state atom. Their potential energy curves are nearly flat on the scale of Fig. 1. Two additional adiabatic potential energy curves split away from the degenerate Rydberg manifold. Loosely speaking, each of these can be associated with the interaction channels given by the two terms in Eq. (18). The resulting s-wave-dominated and p-wave-dominated molecular states are called trilobite and butterfly states, respectively [1,36]. These two states have a prominent avoided crossing [37] shown in the inset. Nonadiabatic effects are expected to be strongest in its vicinity.

Based on this Rydberg level structure, the adiabatic eigenstates ψ_1 and ψ_2 defining the potentials V_1 and V_2 shown in Fig. 1 are subject to several changes in the dominant electronic character. Three avoided crossings occur for V_1 (solid blue). Starting asymptotically at large R, V_1 has dominant F-state character. Going inward towards smaller R values, firstly V_1 attains trilobite character, secondly attains butterfly character, and lastly, at much lower energies, attains S-state character. For V_2 on the other hand (solid red), four avoided crossings occur. Starting asymptotically at large R, V_2 has dominant trilobite character. Going inward towards smaller R values, firstly V_2 attains F-state character, secondly attains butterfly character, thirdly attains trilobite character, and lastly attains F-state character once more.

We obtain converged results for the vibronic spectra in the examined energy ranges shown in the following sections by selecting only these two adiabatic states for the calculation. No deviations were found between these calculations and those performed with three and four channels, including also the asymptotic S and F adiabatic potentials shown in Fig. 1. Additionally, to obtain molecular states, we set a variable hard-wall boundary at small R_0 and average the results over 50 different R_0 values. This is the stabilization method established for ultralong-range molecules in Ref. [20].

B. Variation of the electronic structure

Let us consider how the adiabatic potential energy curves, the off-diagonal derivative coupling element, and the diabatic potential curves vary as a function of n. These quantities are plotted in Fig. 2. The derivative coupling element $P_{\alpha\alpha'}$ is a prefactor to a derivative operator of the vibrational degree of freedom in the total Schrödinger equation, Eq. (4). Therefore multiplying $P_{\alpha\alpha'}$ by a unit length and dividing by the molecule's reduced mass results in a unit of energy, allowing us to show it alongside the electronic adiabatic potential energy curves. Hence we can compare the relative strengths of nonadiabatic couplings for molecules at different n.

All of the avoided crossings discussed previously are accompanied by signatures in the derivative coupling element P_{12}, shown as solid green line. Note, for example, the peak at the outermost avoided crossing at large R. The most unusual feature of P_{12} is its large value over the entire range where the two adiabatic states have trilobite and butterfly character, even when the potential curves are relatively well separated in energy. P_{12} displays its most significant feature near the avoided crossing, where it either has one or two sharp peaks, depending on the principal quantum number. At $n = 43$, in the leftmost subfigure we find a symmetric double-peak structure in P_{12}. At $n = 44$, in the middle subfigure, we find a very sharp peak in P_{12} that extends beyond the range of the figure. Specifically here, a treatment in the adiabatic representation becomes impossible, because the functional behavior of the coupling elements cannot be accurately represented on a feasible radial grid. At $n = 45$, in the rightmost subfigure, we find an asymmetric double-peak structure in P_{12}. These are the main characteristics of the derivative coupling element for the two underlying adiabatic states over the full range of
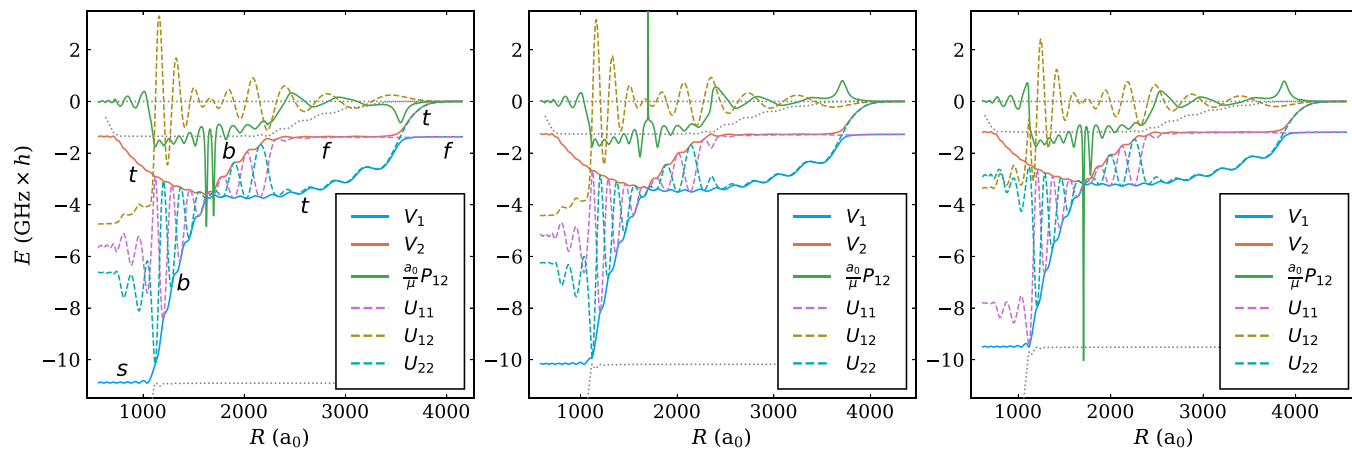
FIG. 2. Adiabatic potential energy curves V_1, V_2, the off-diagonal derivative coupling element P_{12}, and the diabatic potential matrix elements U_{11}, U_{12}, and U_{22} for principal quantum numbers $n = 43$–45 (left to right). Other adiabatic potentials are printed as gray, dotted lines, additional labels as in Fig. 1. Energies are given relative to the degenerate atomic Rydberg level.

n between 25 and 70. The patterns repeat in increments of approximately 3–4 n levels. In the case of a single sharp peak, the avoided crossing of the two potentials becomes extremely narrow. This is remarkable given the overall energies of the molecular system. It resembles the cases of conical intersections discussed in Ref. [14]. Due to the singular character of the coupling elements, methods to solve the total Hamiltonian (1) that rely on the adiabatic representation fail. It is useful to transform to the diabatic representation.

The elements of the diabatic potential matrix are shown as dashed lines in Fig. 2. The diagonal elements (diabatic potential curves) are shown in purple and blue, and the off-diagonal coupling is depicted in beige. Notably, over all regions where the dominant character of the adiabatic states are trilobite and butterfly, all elements of the diabatic potential matrix have strong oscillatory character. As the rotation angle of the transformation between the adiabatic and diabatic representation is the integral of the derivative coupling element P_{12}, this behavior may not seem surprising. After all, P_{12} is large in that entire region. It is, however, rather unusual, as the diabatic potentials do not provide any physical intuition for the molecular system. The oscillatory behavior is known, however, to occur for states which are coupled by a large dipole transition element [43]. This is certainly true for the trilobite and butterfly state. We notice that the n-dependent structure of the derivative coupling element does not have a significant influence on the structure of the diabatic potential matrix elements. A simplified model, including only trilobite and butterfly and neglecting quantum defect states, is studied in Appendix A reproducing these diabatic potentials. The strange behavior of the diabatic potentials poses no problem for a numerical solution of the coupled channel problem. In regimes where the derivative coupling elements are nonsingular, it yields identical results as the adiabatic representation. When nearly singular couplings make the adiabatic representation unstable numerically, the diabatic representation is not at all affected.

The overall magnitude of the nonadiabatic coupling elements, both for $P_{\alpha\alpha'}$ and $Q_{\alpha\alpha'}$, is approximately constant across all n. On the other hand, the energies of the adiabatic potentials scale as n^{-3}, in line with the scaling of the level

splittings in Rydberg atoms. As a result, nonadiabatic effects play a more important role at large n. The diagonal scalar coupling terms lead to an overall energy shift of the potentials on the order of 5 MHz. At low $n \lesssim 30$, this is more or less negligible. However, at large $n \gtrsim 60$, this shift is larger than the energy spacing of molecular states. Figure 3 shows the adiabatic potentials for $n = 65$ as solid lines along with the Born-Huang corrected potentials, which include the diagonal scalar coupling, as dashed lines. The lower inset shows that the Born-Huang terms give rise to a correction on the order of 5 MHz, which leads to a significant overall shift of the molecular states. Additionally, the upper inset shows the potential barrier that appears at the narrow avoided crossing due to these diagonal nonadiabatic coupling terms. This barrier is a result of the narrow energy gap of the two states at the
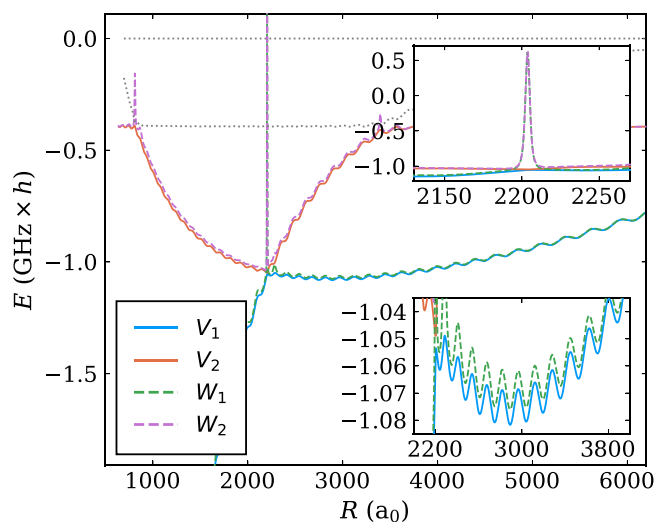

FIG. 3. Adiabatic potential energy curves V_1, V_2, and Born-Huang corrected potentials W_1, W_2 for principal quantum number $n = 65$. The insets show zooms of relevant regions. Energies are given relative to the degenerate atomic Rydberg level.
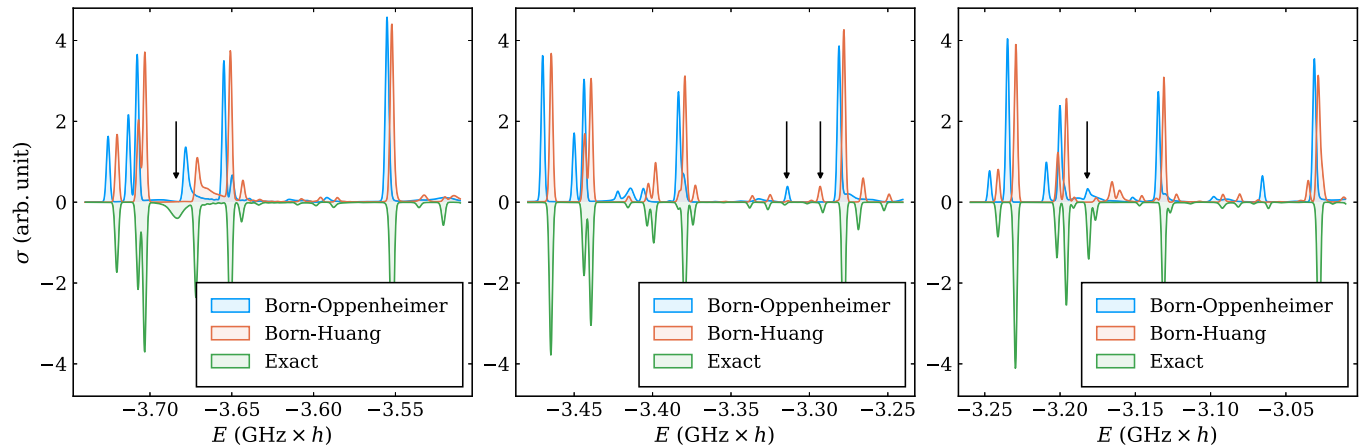
FIG. 4. Simulated absorption spectra employing a single channel neglecting (including) scalar coupling, i.e., using Born-Oppenheimer (Born-Huang) potentials, and employing coupled channels for principal quantum numbers $n = 43$–45 (left to right). Markers correspond to specific states shown in Fig. 5. Energies are given relative to the degenerate atomic Rydberg level.

crossing and the correspondingly sharply peaked derivative coupling element.

C. Vibrational structure and molecular spectrum

Let us now turn to the energy eigenfunctions of the total Hamiltonian (1). Figure 4 shows the simulated spectral signal obtained from the total wave functions depending on the underlying model: in blue, the single-channel model using the adiabatic potential energy curves V_1 and V_2, the Born-Oppenheimer spectrum; in orange, the single-channel model using the Born-Huang corrected potential energy curves W_1 and W_2, which include the diagonal scalar couplings Q_{11} and Q_{22}, the Born-Huang spectrum; and in green (mirrored for visibility), the two-channel model in the diabatic representation, the exact spectrum.

Two features are immediately striking. Firstly, both the Born-Huang spectrum and the exact spectrum are shifted in energy compared to the Born-Oppenheimer spectrum. Secondly, the Born-Huang spectrum reproduces the exact spectrum quite accurately over most of the energy range. This clearly shows the importance of including at least the diagonal nonadiabatic couplings for investigations of ultralong-range Rydberg molecules. That said, we do find signals in the exact spectrum that have no counterpart in the single-channel spectra. At $n = 43$, in the leftmost subfigure, around $E = -3.68$ GHz there is a broad peak (highlighted by a marker) next to a sharp peak with rather strong signal. The single-channel spectra only show a single asymmetric peak of weaker signal. At around $E = -3.51$ GHz, there is a weak peak in the exact signal not found in the single-channel spectra. At $n = 44$, in the middle subfigure, the Born-Huang spectrum is astonishingly accurate. Some of the peaks with weaker signal are slightly shifted towards higher energies compared to the exact spectrum. At $n = 45$, in the rightmost subfigure, at around $E = -3.18$ GHz the exact spectrum features a double-peak structure (highlighted by a marker) significantly shifted from a similar but weaker in signal double-peak in the Born-Huang spectrum. Interestingly, the Born-Oppenheimer spectrum predicts a single peak at the

correct energy. Between $E = -3.03$ and $E = -3.07$ GHz, the single-channel spectra each predict a peak completely absent in the exact spectrum.

D. Off-diagonal nonadiabatic couplings

Some of these spectral features have their origin in strong off-diagonal nonadiabatic couplings that cannot be described in a single-channel model. In order to gain a better understanding of these situations, we now turn to study the molecular wave functions directly. Figure 5 shows selected molecular eigenstates after tracing over the electronic degree of freedom, shifted according to their eigenenergies. The corresponding squared wave functions can be interpreted as vibrational probability distributions. Here, states that are strongly suppressed in the spectra due to their vanishing Franck-Condon overlaps are not shown. This holds also for states resembling box states, which are artifacts related to the inner hard-wall boundary. The energy window is the same as that for the spectra plotted in Fig. 4. The gray curves represent the adiabatic potentials V_1 and V_2 shown in Fig. 2. Additionally, the black curves represent the Born-Huang corrected potentials W_1 and W_2. In line with the color scheme used in Fig. 4, the eigenstates are obtained from the different models: Born-Oppenheimer states in blue, Born-Huang states in orange, and exact states in green. As the spectra suggest, most of the molecular wave functions obtained from the different models do not differ strongly. For example, the states that localize in the individual potential wells of the trilobite potential only deviate in energy. These are the states that correspond to strong signals in Fig. 4. Molecular states that have no counterpart in a different model localize in the vicinity of the avoided crossing where nonadiabatic couplings are particularly strong; these are located in the leftmost region of each subfigure.

For $n = 43$, in the leftmost subfigure, most notably around $E = -3.68$ GHz, a molecular state localizes at around $R = 1650 \, a_0$ (highlighted by a marker). Although this state appears to be trapped in the Born-Huang potential well, the lack of a corresponding Born-Huang state shows that the potential well alone is not suitable to support such a state.
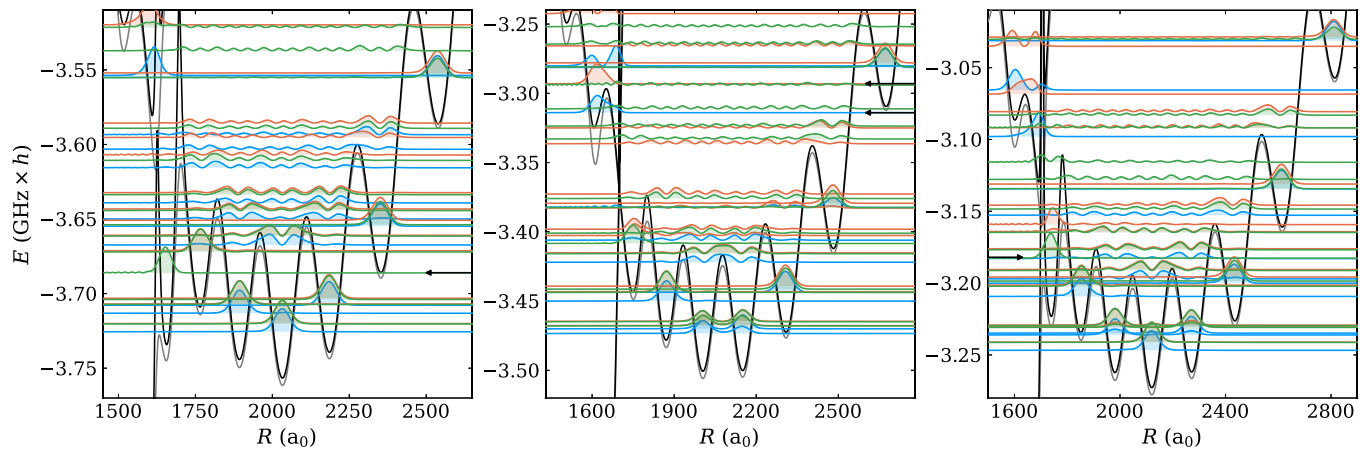
FIG. 5. Selected molecular eigenstates obtained using a single-channel calculation excluding (blue) and including (orange) scalar coupling, as well as those from the two coupled channel calculations (green). The Born-Oppenheimer (gray) and Born-Huang (black) potentials for principal quantum numbers $n = 43$–45 (left to right) are also shown. These states correspond to the spectral signals shown in Fig. 4, including some states highlighted with markers. Energies are given relative to the degenerate atomic Rydberg level.

In other words, this molecular state is trapped nonadiabatically by the off-diagonal derivative couplings. The exact state has a very small but finite amplitude towards small R, resembling states trapped by internal quantum reflection, discussed extensively throughout the literature on ultralong-range Rydberg molecules [19–21]. At higher energy, around $E = -3.55$ GHz, and at similar internuclear distance, there is a Born-Oppenheimer state localizing in a potential well that is shifted upwards by the Born-Huang correction. This state cannot be identified in the spectrum because it is degenerate in energy with molecular states localizing at large internuclear distances, around $R = 2500$ a_0, where nonadiabatic couplings are generally much weaker. The corresponding Born-Huang state is at approximately $E = -3.53$ GHz, barely visible in the figure. There is no exact counterpart to these states. In other words, these states are subject to rapid nonadiabatic decay into the continuum of the lower potential. At $n = 44$, in the middle subfigure, the only region with significant differences between different models is again the potential formed by the avoided crossing, where single-channel states localize (highlighted by markers) but exact states do not occur. At $n = 45$, in the rightmost subfigure, the overall structure is very similar to $n = 43$.

To summarize the most important observations here, we find that the potential well formed by the avoided crossing of the trilobite and butterfly does not support localized molecular bound states, as would be suggested by single-channel calculations. This is in marked contrast to other types of Rydberg molecules, most prominently, Rydberg macrodimers, where a potential well is formed by the crossing of induced dipole potentials, and in charged Rydberg molecules, where a potential well is formed by the crossing of an attractive polarization potential and a repulsive dipole potential. Both of these cases are known to support bound molecular states [6,11]. In ultralong-range Rydberg molecules, nonadiabatic couplings are too strong for such states to exist. On the other hand, nonadiabatic couplings can lead to the formation of quantum-reflection-type states at the same radial position but at energies much lower than the potential well. Counterin-

tuitively, both the observed effects, nonadiabatic decay and nonadiabatic trapping, are more pronounced at principal quantum numbers where the derivative coupling element features a double-peak structure. In the case of a single narrow peak of P_{12}, such effects are less significant. We attribute this to the fact that nonadiabatic couplings are strongly pronounced over a much wider range of R in double-peak situations. Opposed to this, the single peak can become arbitrarily narrow. Its integral converges at $\frac{\pi}{2}$, corresponding to a complete inversion of the adiabatic character.

Overall, the vibronic effects described in this section are not limited to the quantum numbers $n = 43$–45. On the contrary, we find similar patterns over a wide range of n. Independent of n, the total energy shift between exact molecular states and states obtained within the Born-Oppenheimer approximation is approximately 5 MHz. For states localizing in the vicinity of the avoided crossing, the shift can be much larger. Vibronic interaction effects are less pronounced at principle quantum numbers featuring highly singular P-matrix elements resembling conical intersections.

IV. CONCLUSIONS AND OUTLOOK

We have studied vibronic interaction effects in ultralong-range Rydberg molecules focusing on trilobite and butterfly states. The avoided crossing between these two states gives rise to nonadiabatic trapping of molecular states including internal quantum reflection resonances. Nonadiabatic decay is also observed. Overall, nonadiabatic corrections to the adiabatic molecular structure lead to energy shifts of spectral lines on the MHz scale. Similar energy shifts in theoretical potential energy curves can be caused by small changes in the scattering lengths, an input into the calculation, or by finite-size basis effects [44]. As such, comparison with experiment has been useful to help benchmark convergence in the basis or to adjust scattering lengths. Although this was done for different molecular states than those studied here, our results show that care must be taken in such endeavors in order to avoid misattributing nonadiabatic effects to these other causes.

This work opens a pathway to study nonadiabatic interaction effects in Rydberg molecules. We consider multiple scenarios to be of high relevance: Firstly, nonadiabatic decay of molecular states correlated to Rydberg quantum defect states. This is important to understand molecular lifetimes. Secondly, nonadiabatic effects are naturally more pronounced in lighter molecules such as Li*Li, Li*Rb, or Na*Na, where they might lead to more striking effects. Thirdly, the methods developed for this study can be applied to other species of Rydberg molecules such as charged molecules and macrodimers. Lastly, exposing molecules to additional external fields is a promising perspective, especially as the gap between trilobite and butterfly curves can be controlled by an external electric field [45]. It may lead to more control of molecular properties while causing more complexity, such as many-state interaction dynamics.

Notably, in the scenario considered here, the molecular channels are coupled but closed. In ultralong-range Rydberg molecules, however, scenarios can be investigated involving open and closed channels. This introduces coupling to continuum states and can lead, for example, to Feshbach resonances. In general, Rydberg molecules are highly asymmetric and imbalanced objects. Similar systems are encountered in semiconductor materials based on Rydberg excitons. Their nonadiabatic interaction effects may lead to unexpected material response properties.

ACKNOWLEDGMENTS

APPENDIX A: NEGLECTING QUANTUM DEFECT STATES

To highlight the counterintuitive structure of the diabatic potential curves in the case of the trilobite and butterfly, Fig. 6 shows potentials in an artificial setup. Here all quantum defects of rubidium have been set to zero. This can also be interpreted as the electronic structure of H*Rb molecules. Only two nontrivial adiabatic eigenstates remain: the trilobite and the butterfly (solid curves). The diabatic potentials (dotted curves) are oscillatory over the full range of R. The P-matrix element of these two states is large over the full range of R leading to this behavior. This is related to the fact that the two states have an extremely large dipole transition element, orders of magnitude larger than for low-angular-momentum states [37,39].

APPENDIX B: DIPOLE DIABATIZATION

Another way to represent the coupled system of equations (4) is diabatization by aid of diagonalizing the electronic
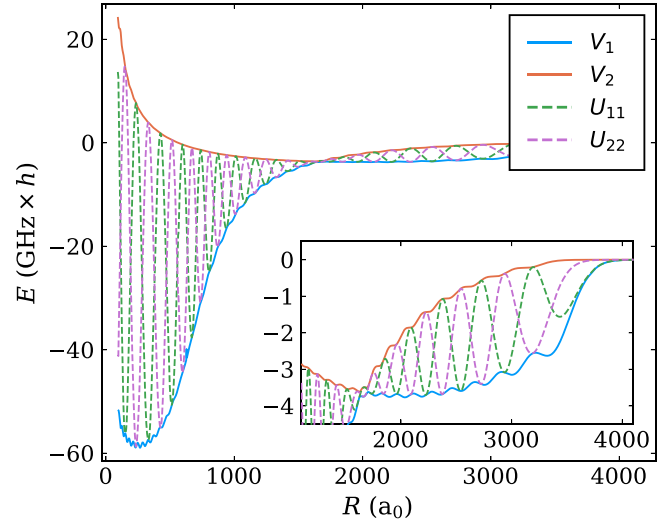

FIG. 6. Adiabatic potential energy curves V_1, V_2 and the diagonal diabatic potential matrix elements U_{11}, U_{22} for principal quantum number $n = 43$, neglecting quantum defect states. The inset shows a zoom. Energies are given relative to the degenerate atomic Rydberg level.

dipole transition matrix, i.e., the position operator

$$D_{\alpha\alpha'} = \int d\mathbf{r}\, \mathbf{r} \psi_\alpha^*(\mathbf{r}; R) \psi_{\alpha'}(\mathbf{r}; R). \tag{B1}$$

The goal is to find a representation of the electronic basis that is dipole decoupled. Diagonalizing $\hat{\mathbf{D}}(R)$ equips us with a transformation $\bar{\mathbf{S}}(R)$ between the adiabatic and the dipole diabatic representation. It is defined via

$$\hat{\mathbf{d}} = \bar{\mathbf{S}}^\dagger \hat{\mathbf{D}} \bar{\mathbf{S}}, \tag{B2}$$

where $\hat{\mathbf{d}}(R)$ is a diagonal matrix. The Schrödinger equation becomes

$$\left[\frac{-\nabla_R^2}{2\mu} + \bar{U} - E \right] \bar{\chi} = \frac{1}{2\mu} \bar{\mathbf{\Lambda}} \bar{\chi}, \tag{B3}$$

where $\bar{\chi} = \bar{\mathbf{S}}^\dagger \chi$, $\bar{U} = \bar{\mathbf{S}}^\dagger \hat{V} \bar{\mathbf{S}}$, and $\bar{\mathbf{\Lambda}} = \bar{\mathbf{S}}^\dagger \hat{\mathbf{\Lambda}} \bar{\mathbf{S}}$. While this is formally equivalent to Eqs. (4) and (15), the point of this representation is that residual couplings $\bar{\mathbf{\Lambda}}$ are expected to be small, such that the right-hand side of this equation is set to zero. In the following we will show that this is not an accurate assumption in our setup.

APPENDIX C: HYBRIDIZED BASIS

The dipole diabatic representation is closely related to another approach originating in results found in Refs. [46,47] and developed previously in Refs. [41,48,49]. Here a hybridized electronic basis employing analytic functions of the trilobite and butterfly states

$$|1\rangle = \frac{1}{T} \sum_\beta \phi_\beta(R) \phi_\beta(\mathbf{r}), \tag{C1}$$

$$|2\rangle = \frac{1}{B} \sum_\beta \phi_\beta'(R) \phi_\beta(\mathbf{r}), \tag{C2}$$
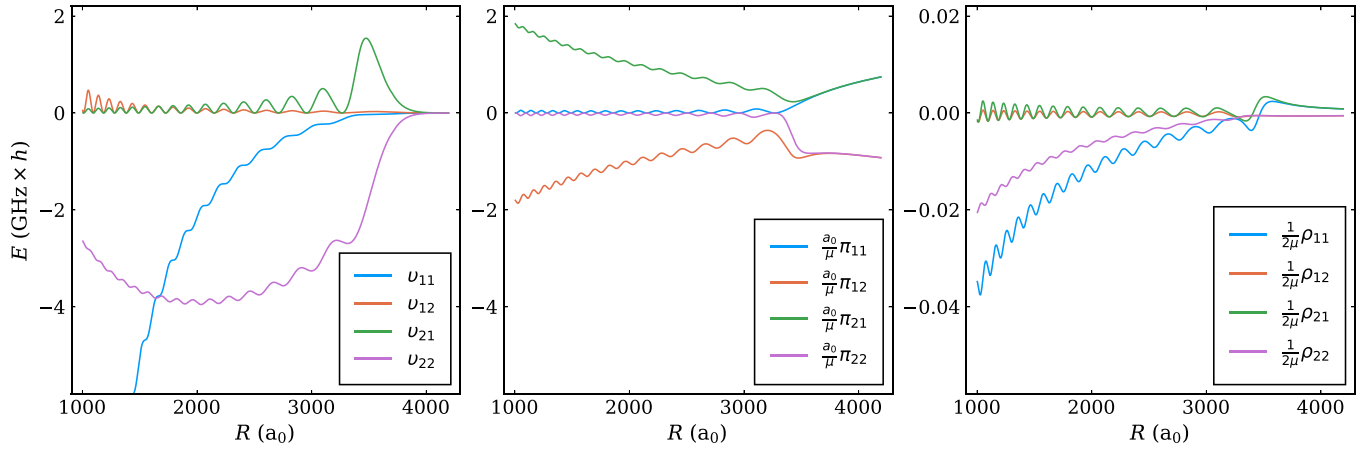
FIG. 7. Potential energy curves $\upsilon_{\kappa\kappa'}$ (left), derivative $\pi_{\kappa\kappa'}$ (middle), and scalar coupling elements $\rho_{\kappa\kappa'}$ (right) for principal quantum number $n = 43$ obtained via the hybridized basis approach. Energies are given relative to the degenerate atomic Rydberg level.

with two (R-dependent) normalization constants $T^2 = \sum_\beta |\phi_\beta|^2$ and $B^2 = \sum_\beta |\phi'_\beta|^2$, is used to expand the total wave function. This ansatz suffers from the fact that the two basis states are not orthogonal. In fact, for large R they become linearly dependent. The off-diagonal overlap matrix element here is $\langle 1|2\rangle = \frac{M^2}{TB}$, where $M^2 = \sum \phi'(R)\phi(R)$. Still, the resulting potential and nonadiabatic coupling terms provide some intuitive understanding of the physical situation. Employing the hybridized basis, the total Schrödinger equation contains a nondiagonal potential matrix,

$$\hat{\upsilon} = \sum_{\kappa\kappa'} O_{\kappa\kappa'}^{-1} \langle \kappa|V_{ea}|\kappa'\rangle = \begin{pmatrix} a_s T^2 & a_s \frac{T}{B} M^2 \\ a_p \frac{B}{T} M^2 & a_p B^2 \end{pmatrix}, \quad \text{(C3)}$$

where $\kappa = \{1, 2\}$ labels the two basis states, and $O_{\kappa\kappa'}^{-1}$ is the matrix element of the inverse overlap matrix. The potential curves in $\hat{\upsilon}$ almost exactly reproduce the dipole diabatic potentials for the trilobite and butterfly states in $\bar{U}$. We attribute the slight differences merely to the fact that dipole diabatization provides an orthogonal basis. The elements of $\hat{\upsilon}$ are shown in Fig. 7 on the left. Although this approach reduces the singularity of nonadiabatic couplings, they remain nonzero in this approach. The derivative coupling matrix,

$$\hat{\pi} = \sum_{\kappa\kappa'} O_{\kappa\kappa'}^{-1} \langle \kappa|\nabla_R|\kappa'\rangle$$

$$= \begin{pmatrix} -\frac{M^2(\tilde{M}^2 - M^2 N^2/B^2)}{T^2 B^2 - M^4} & \frac{B}{T} \\ \frac{TB(\tilde{M}^2 - M^2 N^2/B^2)}{T^2 B^2 - M^4} & -\frac{M^2}{T^2} \end{pmatrix}, \quad \text{(C4)}$$

is not anti-Hermitian due the nonorthogonality of the underlying basis states. The additional terms encountered in this expression are $\tilde{M}^2 = \sum \phi''(R)\phi(R)$ and $N^2 = \sum \phi''(R)\phi'(R)$. For the same reason, the scalar coupling matrix $\hat{\rho}$ does not obey the usual relation (9). In fact, given this nonorthogonal basis, it is not clear how to analytically obtain a transformation to the adiabatic representation. After all, this transformation is not unitary at large R. While the analytic matrix elements of the potential and couplings are not straightforward, they all result in smooth functions of R and n, which are shown in Fig. 7. Notably, the derivative coupling elements (middle) become large asymptotically at large R.

APPENDIX D: ADIABATIC TO DIABATIC TRANSFORMATIONS

The unitary transformation between adiabatic and diabatic representation can be found analytically, as long as there is only a single adiabatic parameter (in our case R). As these transformations are often useful, however, to our knowledge typically not provided in the literature, we reproduce here the explicit transformations for three- and four-channel systems. Considering three adiabatic states, the unitary transformation is a general rotation in three dimensions that can be expressed via three angles, e.g., the Euler angles. Here we choose

$$\hat{S}_{3D}(R) = \hat{R}_Z(\alpha) \cdot \hat{R}_X(\pi/2 - \beta) \cdot \hat{R}_Z(\gamma), \quad \text{(D1)}$$

where $\hat{R}_i(\varphi)$ is a rotation in three dimensions around the axis i by the angle φ. Solving Eq. (14) for a general three-state P matrix,

$$\hat{P}_{3D} = \begin{pmatrix} 0 & p_{12} & p_{13} \\ -p_{12} & 0 & p_{23} \\ -p_{13} & -p_{23} & 0 \end{pmatrix}, \quad \text{(D2)}$$

leads to a set of coupled differential equations for the three angles α, β, and γ:

$$\alpha' = p_{12} - \tan\beta \, (p_{13}\cos\alpha + p_{23}\sin\alpha), \quad \text{(D3)}$$

$$\beta' = p_{13}\sin\alpha - p_{23}\cos\alpha, \quad \text{(D4)}$$

$$\gamma' = \sec\beta \, (p_{13}\cos\alpha + p_{23}\sin\alpha). \quad \text{(D5)}$$

This approach extends to higher-dimensional systems. A general rotation in d dimensions can be characterized by $d(d-1)/2$ angles governing simple rotations that leave a $(d-2)$-dimensional subspace unchanged.

In four dimensions, general rotations are parameterized by six angles. The derivation and solution of the corresponding differential equations gets increasingly involved for more

states. Let's call the four axes in four dimensions $\{w, x, y, z\}$, then simple rotations leave a plane unchanged. Say $\hat{\boldsymbol{R}}_{ij}(\theta)$ is a rotation of angle θ in the i-j-plane, e.g.,

$$\hat{\boldsymbol{R}}_{wy} = \begin{pmatrix} \cos\theta & 0 & -\sin\theta & 0 \\ 0 & 1 & 0 & 0 \\ \sin\theta & 0 & \cos\theta & 0 \\ 0 & 0 & 0 & 1 \end{pmatrix}. \tag{D6}$$

We choose (somewhat arbitrary) an ansatz for a unitary matrix allowing general rotations in four dimensions as

$$\hat{\boldsymbol{S}}_{4D} = \hat{\boldsymbol{R}}_{wx}(\alpha) \cdot \hat{\boldsymbol{R}}_{wy}(\beta) \cdot \hat{\boldsymbol{R}}_{wz}(\gamma) \cdot \hat{\boldsymbol{R}}_{xy}(-\delta) \cdot \hat{\boldsymbol{R}}_{xz}(\epsilon) \cdot \hat{\boldsymbol{R}}_{yz}(\zeta) \tag{D7}$$

and the general P matrix

$$\hat{\boldsymbol{P}}_{4D} = \begin{pmatrix} 0 & p_{12} & p_{13} & p_{14} \\ -p_{12} & 0 & p_{23} & p_{24} \\ -p_{13} & -p_{23} & 0 & p_{34} \\ -p_{14} & -p_{24} & -p_{34} & 0 \end{pmatrix}. \tag{D8}$$

The angle α mixes P-matrix elements, leading to the following shorthand notations:

$$a_3^- = p_{13} \sin\alpha - p_{23} \cos\alpha, \tag{D9}$$

$$a_4^- = p_{14} \sin\alpha - p_{24} \cos\alpha, \tag{D10}$$

$$a_3^+ = p_{13} \cos\alpha + p_{23} \sin\alpha, \tag{D11}$$

$$a_4^+ = p_{14} \cos\alpha + p_{24} \sin\alpha, \tag{D12}$$

and likewise for β:

$$b^- = a_4^+ \sin\beta - p_{34} \cos\beta, \tag{D13}$$

$$b^+ = a_4^+ \cos\beta + p_{34} \sin\beta, \tag{D14}$$

and likewise for δ:

$$d^- = b^- \sin\delta - a_4^- \cos\delta, \tag{D15}$$

$$d^+ = b^- \cos\delta + a_4^- \sin\delta, \tag{D16}$$

such that the following set of differential equations is obtained for the six angles:

$$\alpha' = p_{12} + a_3^- \tan\beta + a_4^- \sec\beta \tan\gamma, \tag{D17}$$

$$\beta' = a_3^+ + b^- \tan\gamma, \tag{D18}$$

$$\gamma' = b^+, \tag{D19}$$

$$\delta' = a_3^- \sec\beta + a_4^- \tan\beta \tan\gamma - d^- \sec\gamma \tan\epsilon, \tag{D20}$$

$$\epsilon' = -d^+ \sec\gamma, \tag{D21}$$

$$\zeta' = d^- \sec\gamma \sec\epsilon. \tag{D22}$$

[1] C. H. Greene, A. S. Dickinson, and H. R. Sadeghpour, Creation of Polar and Nonpolar Ultra-Long-Range Rydberg Molecules, Phys. Rev. Lett. **85**, 2458 (2000).

[2] V. Bendkowsky, B. Butscher, J. Nipper, J. P. Shaffer, R. Löw, and T. Pfau, Observation of ultralong-range Rydberg molecules, Nature (London) **458**, 1005 (2009).

[3] C. Fey, F. Hummel, and P. Schmelcher, Ultralong-range Rydberg molecules, Mol. Phys. **118**, e1679401 (2020).

[4] M. Deiß, S. Haze, and J. Hecker Denschlag, Long-range atom–ion Rydberg molecule: A novel molecular binding mechanism, Atoms **9**, 34 (2021).

[5] A. Duspayev, X. Han, M. A. Viray, L. Ma, J. Zhao, and G. Raithel, Long-range Rydberg-atom–ion molecules of Rb and Cs, Phys. Rev. Res. **3**, 023114 (2021).

[6] N. Zuber, V. S. V. Anasuri, M. Berngruber, Y.-Q. Zou, F. Meinert, R. Löw, and T. Pfau, Observation of a molecular bond between ions and Rydberg atoms, Nature (London) **605**, 453 (2022).

[7] C. Boisseau, I. Simbotin, and R. Côté, Macrodimers: Ultralong Range Rydberg Molecules, Phys. Rev. Lett. **88**, 133004 (2002).

[8] K. Overstreet, A. Schwettmann, J. Tallant, D. Booth, and J. P. Shaffer, Observation of electric-field-induced Cs Rydberg atom macrodimers, Nat. Phys. **5**, 581 (2009).

[9] H. Saßmannshausen and J. Deiglmayr, Observation of Rydberg-Atom Macrodimers: Micrometer-Sized Diatomic Molecules, Phys. Rev. Lett. **117**, 083401 (2016).

[10] Y.-Q. Zou, M. Berngruber, V. S. V. Anasuri, N. Zuber, F. Meinert, R. Löw, and T. Pfau, Observation of Vibrational Dynamics of Oriented Rydberg-Atom-Ion Molecules, Phys. Rev. Lett. **130**, 023002 (2023).

[11] S. Hollerith, J. Zeiher, J. Rui, A. Rubio-Abadal, V. Walther, T. Pohl, D. M. Stamper-Kurn, I. Bloch, and C. Gross, Quantum gas microscopy of Rydberg macrodimers, Science **364**, 664 (2019).

[12] A. Duspayev and G. Raithel, Nonadiabatic decay of Rydberg-atom–ion molecules, Phys. Rev. A **105**, 012810 (2022).

[13] M. Schlagmüller, T. C. Liebisch, F. Engel, K. S. Kleinbach, F. Böttcher, U. Hermann, K. M. Westphal, A. Gaj, R. Löw, S. Hofferberth, T. Pfau, J. Pérez-Ríos, and C. H. Greene, Ultracold Chemical Reactions of a Single Rydberg Atom in a Dense Gas, Phys. Rev. X **6**, 031020 (2016).

[14] F. Hummel, M. T. Eiles, and P. Schmelcher, Synthetic Dimension-Induced Conical Intersections in Rydberg Molecules, Phys. Rev. Lett. **127**, 023003 (2021).

[15] D. A. Anderson, S. A. Miller, and G. Raithel, Photoassociation of Long-Range nD Rydberg Molecules, Phys. Rev. Lett. **112**, 163201 (2014).

[16] H. Saßmannshausen, F. Merkt, and J. Deiglmayr, Experimental Characterization of Singlet Scattering Channels in Long-Range Rydberg Molecules, Phys. Rev. Lett. **114**, 133201 (2015).

[17] F. Böttcher, A. Gaj, K. M. Westphal, M. Schlagmüller, K. S. Kleinbach, R. Löw, T. C. Liebisch, T. Pfau, and S. Hofferberth, Observation of mixed singlet-triplet Rb$_2$ Rydberg molecules, Phys. Rev. A **93**, 032512 (2016).

[18] J. L. MacLennan, Y. J. Chen, and G. Raithel, Deeply bound $(24D_J + 5S_{1/2})$ ^{87}Rb and ^{85}Rb molecules for eight spin couplings, Phys. Rev. A **99**, 033407 (2019).

[19] F. Engel, T. Dieterle, F. Hummel, C. Fey, P. Schmelcher, R. Löw, T. Pfau, and F. Meinert, Precision Spectroscopy of Negative-Ion Resonances in Ultralong-Range Rydberg Molecules, Phys. Rev. Lett. **123**, 073003 (2019).

[20] V. Bendkowsky, B. Butscher, J. Nipper, J. B. Balewski, J. P. Shaffer, R. Löw, T. Pfau, W. Li, J. Stanojevic, T. Pohl, and J. M. Rost, Rydberg Trimers and Excited Dimers Bound by Internal Quantum Reflection, Phys. Rev. Lett. **105**, 163201 (2010).

[21] D. A. Anderson, S. A. Miller, and G. Raithel, Angular-momentum couplings in long-range Rb$_2$ Rydberg molecules, Phys. Rev. A **90**, 062518 (2014).

[22] M. Born and R. Oppenheimer, Zur quantentheorie der molekeln, Ann. Phys. **389**, 457 (1927).

[23] M. Born and K. Huang, *Dynamical Theory of Crystal Lattices* (Oxford University Press, New York, 1954).

[24] H. Köppel, W. Domcke, and L. S. Cederbaum, Multimode molecular dynamics beyond the Born-Oppenheimer approximation, in *Advances in Chemical Physics*, Vol. 57 (John Wiley & Sons, Ltd., New York, 1984), pp. 59–246.

[25] C. H. Greene, P. Giannakeas, and J. Pérez-Ríos, Universal few-body physics and cluster formation, Rev. Mod. Phys. **89**, 035006 (2017).

[26] P. Naidon and S. Endo, Efimov physics: A review, Rep. Prog. Phys. **80**, 056001 (2017).

[27] G. A. Worth and L. S. Cederbaum, Beyond Born-Oppenheimer: Molecular dynamics through a conical intersection, Annu. Rev. Phys. Chem. **55**, 127 (2004).

[28] M. Baer, *Beyond Born-Oppenheimer: Electronic Nonadiabatic Coupling Terms and Conical Intersections* (John Wiley & Sons, Ltd., New York, 2006).

[29] Z. H. Top and M. Baer, Nonadiabatic transitions in chemical reactions: A quantum mechanical study, Chem. Phys. **10**, 95 (1975).

[30] F. T. Smith, Diabatic and adiabatic representations for atomic collision problems, Phys. Rev. **179**, 111 (1969).

[31] T. Pacher, L. S. Cederbaum, and H. Köppel, Approximately diabatic states from block diagonalization of the electronic Hamiltonian, J. Chem. Phys. **89**, 7367 (1988).

[32] A. B. Alekseyev, H.-P. Liebermann, R. J. Buenker, N. Balakrishnan, H. R. Sadeghpour, S. T. Cornett, and M. J. Cavagnero, Spin–orbit effects in photodissociation of sodium iodide, J. Chem. Phys. **113**, 1514 (2000).

[33] W. Li, I. Mourachko, M. W. Noel, and T. F. Gallagher, Millimeter-wave spectroscopy of cold Rb Rydberg atoms in a magneto-optical trap: Quantum defects of the *ns*, *np*, and *nd* series, Phys. Rev. A **67**, 052502 (2003).

[34] E. Fermi, Sopra lo spostamento per pressione delle righe elevate delle serie spettrali, Nuovo Cim. **11**, 157 (1934).

[35] A. Omont, On the theory of collisions of atoms in Rydberg states with neutral particles, J. Phys. France **38**, 1343 (1977).

[36] E. L. Hamilton, C. H. Greene, and H. R. Sadeghpour, Shape-resonance-induced long-range molecular Rydberg states, J. Phys. B: At. Mol. Opt. Phys. **35**, L199 (2002).

[37] M. I. Chibisov, A. A. Khuskivadze, and I. I. Fabrikant, Energies and dipole moments of long-range molecular Rydberg states, J. Phys. B: At. Mol. Opt. Phys. **35**, L193 (2002).

[38] P. Giannakeas, M. T. Eiles, F. Robicheaux, and J. M. Rost, Dressed Ion-Pair States of an Ultralong-Range Rydberg Molecule, Phys. Rev. Lett. **125**, 123401 (2020).

[39] A. A. Khuskivadze, M. I. Chibisov, and I. I. Fabrikant, Adiabatic energy levels and electric dipole moments of Rydberg states of Rb$_2$ and Cs$_2$ dimers, Phys. Rev. A **66**, 042709 (2002).

[40] M. T. Eiles and C. H. Greene, Hamiltonian for the inclusion of spin effects in long-range Rydberg molecules, Phys. Rev. A **95**, 042515 (2017).

[41] M. T. Eiles, Trilobites, butterflies, and other exotic specimens of long-range Rydberg molecules, J. Phys. B: At. Mol. Opt. Phys. **52**, 113001 (2019).

[42] H. Bachau, E. Cormier, P. Decleva, J. E. Hansen, and F. Martín, Applications of b-splines in atomic and molecular physics, Rep. Prog. Phys. **64**, 1815 (2001).

[43] B. D. Esry and H. R. Sadeghpour, Split diabatic representation, Phys. Rev. A **68**, 042706 (2003).

[44] C. Fey, M. Kurz, P. Schmelcher, S. T. Rittenhouse, and H. R. Sadeghpour, A comparative analysis of binding in ultralong-range Rydberg molecules, New J. Phys. **17**, 055010 (2015).

[45] M. Kurz and P. Schmelcher, Electrically dressed ultra-long-range polar Rydberg molecules, Phys. Rev. A **88**, 022501 (2013).

[46] M. Chibisov, A. M. Ermolaev, F. Brouillard, and M. H. Cherkani, New Summation Rules for Coulomb Wave Functions, Phys. Rev. Lett. **84**, 451 (2000).

[47] M. H. Cherkani, F. Brouillard, and M. Chibisov, Summation rules for Coulomb wavefunction products, J. Phys. B: At. Mol. Opt. Phys. **34**, 49 (2001).

[48] M. T. Eiles, J. Pérez-Ríos, F. Robicheaux, and C. H. Greene, Ultracold molecular Rydberg physics in a high density environment, J. Phys. B: At. Mol. Opt. Phys. **49**, 114005 (2016).

[49] M. T. Eiles, C. Fey, F. Hummel, and P. Schmelcher, Triatomic butterfly molecules, J. Phys. B: At. Mol. Opt. Phys. **53**, 084001 (2020).